

1

2

3       **Verification of a non-hydrostatic dynamical core**

4       **using horizontally spectral element vertically finite**

5       **difference method: 2D Aspects**

6

7

8               Suk-Jin Choi<sup>1),\*</sup>, Francis X. Giraldo<sup>2)</sup>, Junghan Kim<sup>1)</sup>, and Seoleun Shin<sup>1)</sup>

9

10              1) Korea institute of atmospheric prediction systems, 4F., 35 Boramae-ro 5-gil,

11                                      Dongjak-gu, Seoul 156-849, Korea

12              2) Department of Applied Mathematics, Naval Postgraduate School, 833 Dyer Road,

13                                      Monterey, CA 93943, USA

14

15

16

17

18                                      April, 2014,

19                                      Submitted to *Monthly Weather Review*

20

21       

---

22       \*Corresponding author address: Dr. Suk-Jin Choi, Korea institute of atmospheric prediction systems, 4F.,

23       35 Boramae-ro 5-gil, Dongjak-gu, Seoul 156-849, Korea. Email: [sj.choi@kiaps.org](mailto:sj.choi@kiaps.org)

24

Report Documentation Page				Form Approved OMB No. 0704-0188	
Public reporting burden for the collection of information is estimated to average 1 hour per response, including the time for reviewing instructions, searching existing data sources, gathering and maintaining the data needed, and completing and reviewing the collection of information. Send comments regarding this burden estimate or any other aspect of this collection of information, including suggestions for reducing this burden, to Washington Headquarters Services, Directorate for Information Operations and Reports, 1215 Jefferson Davis Highway, Suite 1204, Arlington VA 22202-4302. Respondents should be aware that notwithstanding any other provision of law, no person shall be subject to a penalty for failing to comply with a collection of information if it does not display a currently valid OMB control number.					
1. REPORT DATE <b>APR 2014</b>		2. REPORT TYPE		3. DATES COVERED <b>00-00-2014 to 00-00-2014</b>	
4. TITLE AND SUBTITLE <b>Verification of a non-hydrostatic dynamical core using horizontally spectral element vertically finite difference method: 2D Aspects</b>				5a. CONTRACT NUMBER	
				5b. GRANT NUMBER	
				5c. PROGRAM ELEMENT NUMBER	
6. AUTHOR(S)				5d. PROJECT NUMBER	
				5e. TASK NUMBER	
				5f. WORK UNIT NUMBER	
7. PERFORMING ORGANIZATION NAME(S) AND ADDRESS(ES) <b>Naval Postgraduate School, Department of Applied Mathematics, Monterey, CA, 93943</b>				8. PERFORMING ORGANIZATION REPORT NUMBER	
9. SPONSORING/MONITORING AGENCY NAME(S) AND ADDRESS(ES)				10. SPONSOR/MONITOR'S ACRONYM(S)	
				11. SPONSOR/MONITOR'S REPORT NUMBER(S)	
12. DISTRIBUTION/AVAILABILITY STATEMENT <b>Approved for public release; distribution unlimited</b>					
13. SUPPLEMENTARY NOTES					
14. ABSTRACT <b>The non-hydrostatic (NH) compressible Euler equations of dry atmosphere are solved in a simplified two dimensional (2D) slice (X-Z) framework employing a spectral element method (SEM) for the horizontal discretization and a finite difference method (FDM) for the vertical discretization. The SEM uses high-order nodal basis functions associated with Lagrange polynomials based on Gauss-Lobatto-Legendre (GLL) quadrature points. The FDM employs a third-order upwind biased scheme for the vertical flux terms and a centered finite difference scheme for the vertical derivative terms and quadrature. The Euler equations used here are in a flux form based on the hydrostatic pressure vertical coordinate, which are the same as those used in the Weather Research and Forecasting (WRF) model, but a hybrid sigma-pressure vertical coordinate is implemented in this model. We verified the model by conducting widely used standard benchmark tests: the inertia-gravity wave, rising thermal bubble, density current wave, and linear hydrostatic mountain wave. The numerical results demonstrate that the horizontally spectral element vertically finite difference model is accurate and robust. By using the 2D slice model, we effectively show that the combined spatial discretization method of the spectral element and finite difference method in the horizontal and vertical directions, respectively, offers a viable method for the development of a NH dynamical core. The present core provides a practical framework for further development of three-dimensional (3D) non-hydrostatic compressible atmospheric models.</b>					
15. SUBJECT TERMS					
16. SECURITY CLASSIFICATION OF:			17. LIMITATION OF ABSTRACT <b>Same as Report (SAR)</b>	18. NUMBER OF PAGES <b>41</b>	19a. NAME OF RESPONSIBLE PERSON
a. REPORT <b>unclassified</b>	b. ABSTRACT <b>unclassified</b>	c. THIS PAGE <b>unclassified</b>			



## Abstract

The non-hydrostatic (NH) compressible Euler equations of dry atmosphere are solved in a simplified two dimensional (2D) slice (X-Z) framework employing a spectral element method (SEM) for the horizontal discretization and a finite difference method (FDM) for the vertical discretization. The SEM uses high-order nodal basis functions associated with Lagrange polynomials based on Gauss-Lobatto-Legendre (GLL) quadrature points. The FDM employs a third-order upwind biased scheme for the vertical flux terms and a centered finite difference scheme for the vertical derivative terms and quadrature. The Euler equations used here are in a flux form based on the hydrostatic pressure vertical coordinate, which are the same as those used in the Weather Research and Forecasting (WRF) model, but a hybrid sigma-pressure vertical coordinate is implemented in this model. We verified the model by conducting widely used standard benchmark tests: the inertia-gravity wave, rising thermal bubble, density current wave, and linear hydrostatic mountain wave. The numerical results demonstrate that the horizontally spectral element vertically finite difference model is accurate and robust. By using the 2D slice model, we effectively show that the combined spatial discretization method of the spectral element and finite difference method in the horizontal and vertical directions, respectively, offers a viable method for the development of a NH dynamical core. The present core provides a practical framework for further development of three-dimensional (3D) non-hydrostatic compressible atmospheric models.

# 1. Introduction

There is a growing interest in developing highly scalable dynamical cores using numerical algorithms under petascale computers with many cores (with the goal of exascale computing just around the corner). The spectral element method (SEM) has been known as one of the most promising methods with high efficiency and accuracy (Taylor et al. 1997; Giraldo 2001; Thomas and Loft 2002). SEM is local in nature because of having a large on-processor operation count (Kelly and Galdo, 2012). The SEM achieves this high level of scalability by decomposing the physical domain into smaller pieces with a small communication stencil. Also SEM has been shown to be very attractive in achieving high-order accuracy and geometrical flexibility on the sphere (Taylor et al. 1997; Giraldo 2001; Giraldo et al. 2004).

To date, the SEM has been successfully implemented in atmospheric modeling such as in the Community Atmosphere Model – spectral element dynamical core (CAM-SE) (Thomas and Loft 2005) and the scalable spectral element Eulerian atmospheric model (SE-AM) (Giraldo and Rosmond, 2004). These models consider the primitive hydrostatic equations on global grid meshes such as a cubed-sphere tiled with quadrilateral elements using SEM in the horizontal discretization and the finite difference method (FDM) in the vertical. The robustness of the SEM has been illustrated through three-dimensional dry dynamical test cases (Thomas and Loft 2005; Giraldo and Rosmond 2004; Giraldo 2005; Taylor et al. 2007; Lauritzen et al. 2010).

The ultimate objective of our study is to build a 3D non-hydrostatic (NH) model based on the compressible Navier-Stokes equations using the combined horizontally SEM and vertically FDM. Since testing a 3D NH model requires a huge amount of computing resources, studying the feasibility of our approach in 2D is an attractive alternative to the

development of a fully 3D model. This is the case because a 2D slice model effectively can test the practical issues resulting from the vertical discretization and time integration, prior to the construction of a full 3D model. Although we could also discretize the vertical direction with SEM (as is proposed in Kelly and Giraldo 2012 and Giraldo et al. 2013), we choose to use a conservative flux-form finite-difference method for discretization in the vertical direction, which provides an easy way for coupling the dynamics and existing physics packages.

We have developed a dry 2D NH compressible Euler model based on SEM along the x-direction and FDM along the z-direction for this purpose. Hereafter, this is simply referred to as the 2DNH model. We adopt the governing equation formulation proposed by Skamarock and Klemp (2008) (hereafter, SK08) which is used in the Weather Research and Forecasting (WRF) Model. The Euler equations are in flux form based on the hydrostatic pressure vertical coordinate. In SK08, the terrain-following sigma-pressure coordinate is used, but here we employ a hybrid sigma-pressure vertical coordinate. Park et al. (2013) (hereafter, PK13) provides a clue for the equation set in the hybrid sigma-pressure in their appendix, in which the hybrid sigma-pressure coordinate is applied to the hydrostatic primitive equations and can be modified exactly to the sigma-pressure coordinate at the level of the actual coding implementation. Also, we built the 2DNH model using a time-split third-order Runge-Kutta (RK3) for the time discretization, which has been shown to work effectively in the WRF model. We keep the temporal discretization of the model as similar as possible to the WRF model in order to more directly discern the differences related to the discrete spatial operators between the two models. This provides robust tools for development and verification of the 2DNH model.

In this paper, we show the feasibility of the 2DNH model by conducting conventional benchmark test cases as well as focusing on the description of the numerical scheme for the

spatial discretization. We verify the 2DNH by analyzing four test cases: the inertia-gravity wave, rising thermal bubble, density current wave, and linear hydrostatic mountain wave.

The organization of this paper is as follows. The next section describes the governing equations with a definition of the prognostic and diagnostic variables used in our model, in which we present essential changes from SK08. Section 3 contains the description of the temporal and spatial discretization including the spectral element formulation. In Sec. 4, we present the results of the 2DNH model using all four test cases. Finally in Sec. 5 we summarize the paper and propose future directions.

## 2. Governing equations

We adopt the governing equation formulation of SK08. Here we implement the hybrid sigma-pressure coordinate reported by PK13 which considered only the hydrostatic primitive equation. The hybrid sigma pressure coordinate is defined with  $\eta \in [0, 1]$  as

$$p_d = B(\eta)(p_s - p_t) + [\eta - B(\eta)](p_0 - p_t) + p_t \quad (1)$$

where  $p_d$  is the hydrostatic pressure of dry air,  $B(\eta)$  is the relative weighting of the terrain-following coordinate versus the normalized pressure coordinate,  $p_s$ ,  $p_t$ , and  $p_0$  are the hydrostatic surface pressure of dry air, the top level pressure, and a reference sea level pressure, respectively. A more detailed description of the hybrid sigma pressure coordinate can be found in the Appendix of PK13. The definition of the flux variables are

$$(\vec{V}_H, W, \Omega, \Theta) = \mu_d \times (\vec{v}_H, w, \dot{\eta}, \theta) \quad (2)$$

where  $\vec{v}_H = (u, v)$  and  $w$  are the velocities in the horizontal and vertical directions, respectively,  $\dot{\eta} \equiv \frac{\partial \eta}{\partial t}$  is the  $\eta$ -coordinate (contravariant) vertical velocity,  $\theta$  is the

116 potential temperature, and  $\mu_d$  is the mass of the dry air in the layers defined as

$$117 \quad \mu_d(x, y, \eta, t) = \frac{\partial \rho_d}{\partial \eta} = \frac{\partial B(\eta)}{\partial \eta} (\rho_s - \rho_t) + \left[ 1 - \frac{\partial B(\eta)}{\partial \eta} \right] (\rho_0 - \rho_t). \quad (3)$$

118 The flux-form Euler equations for dry atmosphere are expressed as

$$119 \quad \frac{\partial \vec{V}_H}{\partial t} = -\mu_d (\nabla_\eta \phi' + \alpha_d \nabla_\eta \rho' + \alpha'_d \nabla_\eta \bar{\rho}) - \nabla_\eta \phi \left( \frac{\partial \rho'}{\partial \eta} - \mu'_d \right) - \nabla_\eta \cdot (\vec{V}_H \otimes \vec{V}_H) - \frac{\partial (\Omega \vec{V}_H)}{\partial \eta} + F_{\vec{V}_H}, \quad (4)$$

$$120 \quad \frac{\partial W}{\partial t} = g \left[ \frac{\partial \rho'}{\partial \eta} - \mu'_d \right] - \nabla_\eta \cdot (\vec{V}_H W) - \frac{\partial (\Omega W)}{\partial \eta} + F_W, \quad (5)$$

$$121 \quad \frac{\partial \mu'_d}{\partial t} = \frac{\partial}{\partial t} \left( \frac{\partial \rho'_d}{\partial \eta} \right) = \frac{\partial B(\eta)}{\partial \eta} \frac{\partial \rho'_s}{\partial t} = -\nabla_\eta \cdot \vec{V}_H - \frac{\partial \Omega}{\partial \eta}, \quad (6)$$

$$122 \quad \frac{\partial \phi'}{\partial t} = -\frac{1}{\mu_d} \left[ \vec{V}_H \cdot \nabla_\eta \phi + \Omega \frac{\partial \phi}{\partial \eta} - gW \right], \quad (7)$$

$$123 \quad \frac{\partial \Theta}{\partial t} = -\nabla_\eta \cdot (\vec{V}_H \Theta) - \frac{\partial (\Omega \Theta)}{\partial \eta}, \quad (8)$$

124 where  $\phi$  is the geopotential,  $\alpha_d$  is the inverse density for dry air, and  $F_{V_H}^r$  and  $F_W$   
 125 represent forcing terms of the Coriolis and curvature which we ignore for simplicity. In Eqs.  
 126 (4)-(8), the governing equations are described with perturbation variables such as  
 127  $\rho = \bar{\rho}(\bar{z}) + \rho'$ ,  $\phi = \bar{\phi}(\bar{z}) + \phi'$ ,  $\alpha_d = \bar{\alpha}_d(\bar{z}) + \alpha'_d$ , and  $\rho_s = \bar{\rho}_s(x, y) + \rho'_s$  where the  
 128 variables denoted by overbars are reference state variables that satisfy hydrostatic balance.

129 For completeness, the diagnostic relation for  $\Omega$  is given by integrating Eq. (6)  
 130 vertically from the surface ( $\eta = 1$ ) to the material surface as

$$131 \quad \Omega = -\int_1^\eta \left( \frac{\partial B(\eta)}{\partial \eta} \frac{\partial \rho'_s}{\partial t} + \nabla_\eta \cdot \vec{V}_H \right) d\eta, \quad (9)$$

132 where  $\frac{\partial \rho'_s}{\partial t}$  is obtained by integrating vertically Eq. (6) for the surface ( $\eta = 1$ ) to the top



( $\eta = 0$ ) using a no-flux boundary condition such as  $\Omega|_{\eta=0 \text{ or } 1} = 0$  and the specification of the vertical coordinate such as  $B(\eta = 1) = 1$  and  $B(\eta = 0) = 0$  as

$$\frac{\partial \rho'_s}{\partial t} = - \int_{\eta=0}^{\eta=1} (\nabla \cdot \vec{V}_H) d\eta. \quad (10)$$

The above equation allows  $\rho'_s$  to be evolved forward in time where we then compute  $\mu'_d$  directly from Eq. (5). The diagnostic relation for the dry inverse density is given as

$$\frac{\partial \phi'}{\partial \eta} = -\bar{\mu}_d \alpha'_d - \alpha_d \mu'_d, \quad (11)$$

and the full pressure for dry atmosphere is

$$p = p_0 \left( \frac{R_d \theta}{p_0 \alpha_d} \right)^{c_p/c_v}. \quad (12)$$

This concludes the description of the governing equations used in our model; in the next section we describe the discretization of the continuous form of the governing equations that are used in our model.

### 3. Discretization

#### a. Spatial discretization

##### 1) Horizontal direction

For a given  $\eta$  level, we discretize the horizontal operators using the SEM. Therefore in 2D (X-Z) slice framework we focus on the SEM discrete gradient operator for 1D (x). In SEM, we approximate the solution in non-overlapping elements  $\Omega^e$  as

$$q(x, t) = \sum_{k=1}^{N+1} \psi_k(x) q_N(x_k, t), \quad (13)$$

where  $x_k$  represents  $N + 1$  grid points that correspond to the Gauss-Lobatto-Legendre (GLL) points and  $\psi_k(x)$  are the  $N$  th-order Lagrange polynomials based on the GLL points.

It is noteworthy that the  $\psi_k$  have the cardinal property, i.e., they can be represented as Kronecker delta functions where  $\psi_k$  are zero at all nodal points except  $x_k$  (but are allowed to oscillate between nodal points).

The GLL points  $\xi_k$  in a reference coordinate system  $\xi \in [-1, +1]$  and the associated quadrature weights  $\omega(\xi_k)$ ,

$$\omega(\xi_k) = \frac{2}{N(N+1)} \left[ \frac{1}{P_N(\xi_k)} \right]^2, \quad (14)$$

are introduced for the Gaussian quadrature:

$$\int_{\Omega^e} q \, d\Omega^e = \int_{-1}^{+1} q(\xi) |J(\xi)| \, d\xi \approx \sum_{i=0}^N \omega(\xi_i) q(\xi_i) |J(\xi_i)|, \quad (15)$$

where  $P_N(\xi)$  are the  $N$  th-order Legendre polynomials,  $J = \frac{\partial x}{\partial \xi}$  is the transformation Jacobian, and  $\Omega^e$  represents the non-overlapping elements.

We now introduce the polynomial expansions into our governing equations in the form

$$\text{of} \quad \frac{\partial q}{\partial t} = -F(q), \quad (16)$$

multiply by the basis function as a test function, and integrate to yield a system of ordinary differential equations as such

$$\sum_{n=1}^{N+1} M_{nk}^e \frac{dq_k}{dt} = - \int_{\Psi_e} F \left( \sum_{n=1}^{N+1} \psi_n(\xi) q_n \right) \psi_k \, d\xi, \quad (17)$$

where  $k = 1, 2, \dots, N+1$ ,  $M_{nk}^e$  is the element based mass matrix given as

$$M_{nk}^e = \int_{\Psi_e} \psi_n \psi_k \, d\xi = \omega_n |J_n| \delta_{nk}, \quad (18)$$

and the right-hand side of Eq. (18) is evaluated using Gaussian quadrature of Eq. (16). It is noted that using GLL points for both interpolation and integration results in a diagonal mass

matrix  $M_{nk}^e$ , which means that the inversion of the mass matrix is trivial.

The horizontal derivatives included in the right-hand side of Eq. (17) are evaluated using the analytic derivatives of the basis functions as follows

$$\frac{\partial q}{\partial x} = \frac{\partial q}{\partial \xi} \frac{\partial \xi}{\partial x} = \frac{\partial}{\partial \xi} \left[ \sum_{k=1}^{N+1} \psi_k(\xi) q_k \right] \frac{\partial \xi}{\partial x} = \left[ \sum_{k=1}^{N+1} \frac{\partial \psi_k}{\partial \xi} q_k \right] \frac{1}{|J|}. \quad (19)$$

Note that the non-differential operations, such as cross products, are computed directly at grid points since we use nodal basis functions associated with Lagrange polynomials based on the GLL points. In order to satisfy the equations globally, we use the direct stiffness summation (DSS) operation. For a more detailed description of the SEM, see Giraldo and Rosmond (2004), Giraldo and Restelli (2008), and Kelly and Giraldo (2012).

## 2) Vertical direction

Using a Lorenz staggering, the variables  $\vec{V}_H$ ,  $\Theta$ ,  $\mu$ ,  $\alpha$ ,  $\rho$  are at layer midpoints denoted by  $k = 1, 2, K$  where  $K$  is the total number of layers, and the variables  $W$ ,  $\Omega$ ,  $\phi$  live at layer interfaces defined by  $k + \frac{1}{2}$ ,  $k = 0, 1, K$ , so that  $\eta_{K+1/2} = \eta_{top}$  and  $\eta_{1/2} = \eta_{bottom} = 1$ . Fig. 1 describes the grid points and the allocation of the variables. Here, we

evaluate the vertical advection terms  $\left( \frac{\partial(\Omega \vec{V}_H)}{\partial \eta}, \frac{\partial(\Omega W)}{\partial \eta}, \text{ and } \frac{\partial(\Omega \theta)}{\partial \eta} \right)$  and vertical

derivative terms  $\left( \frac{\partial \rho'}{\partial \eta}, \text{ and } \frac{\partial \phi}{\partial \eta} \right)$ . The former is discretized using the third-order upwind

biased discretization in Hundsdorfer et al. (1995) which is given as

$$\left. \frac{\partial f}{\partial \eta} \right|_k = \frac{f_{k-2} - 8f_{k-1} + 8f_{k+1} - f_{k+2}}{12\Delta\eta} + \text{sign}(\Omega) \frac{f_{k-2} - 4f_{k-1} + 6f_k - 4f_{k+1} + f_{k+2}}{12\Delta\eta}, \quad (20)$$

where  $f$  corresponds to the flux such as  $\Omega \vec{V}_H$ , and  $\Delta\eta = \eta_{k+1/2} - \eta_{k-1/2}$  is the thickness of

the layer. The latter is discretized by the centered finite difference. Likewise the vertical discretization quadrature rules for the calculations of Eqs. (9) and (10) follow the finite difference discretization naturally.

#### b. Temporal discretization

For integrating the equations, we use the time-split RK3 integration technique following the strategy of SK08, in which low-frequency modes due to advective forcings are explicitly advanced using a large time step of the RK3 scheme, but high-frequency modes are integrated over smaller time steps using an explicit forward-backward time integration scheme for the horizontally propagating acoustic/gravity waves and a fully implicit scheme for vertically propagating acoustic waves and buoyancy oscillations (Klemp et al. 2007). This technique has been shown to work effectively within numerous nonhydrostatic models including the WRF model (Skamarock et al. 2008), the Model for Prediction Across Scales (MPAS) (Skamarock et al. 2012), and the Nonhydrostatic Icosahedral Atmospheric Model (NICAM) (Sato et al. 2008).

It is noted that in the procedure of the time-split RK3 integration, the difference between the approach used in this paper and SK08 comes from the vertical coordinate. Since we use the hybrid sigma-pressure coordinate, the equation for  $\rho'_s$  (Eq. (6)) should be first stepped forward in time using the forward-backward differencing on the small time steps, then  $\mu'_d$  can be computed directly from the specification of the vertical coordinate in Eq. (9) and  $\Omega$  is obtained from the vertical integration.

## 4. Test cases

We validate the 2DNH model on four test cases of the linear hydrostatic mountain wave,

density current, inertia-gravity wave, and rising thermal bubble experiments. All cases but the mountain wave experiment do not have analytic solutions. Therefore, for the mountain wave experiment, numerical results of the 2DNH model are compared to analytic solutions (Durrán and Klemp 1983), and for the other experiments, we compare our results to the results of other published papers.

It should be mentioned that the horizontal SEM formulation is able to utilize arbitrary order polynomials per element to represent the discrete spatial operators, but in this paper all the results presented use either 5th or 8th order polynomials. The averaged horizontal grid spacing is defined as

$$\Delta\bar{x} = \frac{\sum_{n=1}^N \Delta x_n}{N} \quad (21)$$

where  $\Delta x_n$  is the internal grid spacing within the element which is regularly spaced in the domain and  $N$  is the number of the interval associated with irregularly spaced GLL quadrature points which is equivalent to the order of the basis polynomials. The average vertical grid spacing is defined in the same way of Eq. (24). Below, we use this convention to define the grid resolution.

#### a. Linear hydrostatic mountain wave test

In order to verify the 2DNH's feasibility to treat surface elevations associated with the vertical terrain-following coordinate, we simulate the linear hydrostatic mountain wave test introduced by Durrán and Klemp (1983) (hereafter, DK83) in which the analytic steady-state solution is provided by using a single-peaked mountain with uniform zonal wind. To compare our results with the analytic and numerical solution shown in DK83, the 2DNH is initialized using the same initial conditions and mountain profile in DK83 and we analyze our results

using the same metrics of DK83.

The mountain profile is given by

$$h(x) = \frac{h_m}{1 + \left( \frac{x - x_c}{a_m} \right)^2} \quad (22)$$

where the half-length of the mountain  $a_m$  is 10 km, the height  $h_m$  is 1 m, and the prescribed center of the profile is 0 km. The Initial temperature is  $T_0 = 250$  K for an isothermal atmosphere with the uniform zonal wind  $\bar{u} = 20$  m/s. In the isothermal case, the

Brunt-Väisälä frequency  $N^2 = g \frac{d(\ln \bar{\theta})}{dz} \approx \frac{g^2}{c_p T_0}$  yields the potential temperature given as

$$\bar{\theta} = \theta_0 e^{\frac{g}{c_p T_0} z}, \quad (23)$$

which is one of the prognostic variables in our model. The domain is defined as  $(x, z) \in [-300, 300] \times [0, 30]$  km<sup>2</sup>. The bottom boundary uses a no-flux boundary condition while the lateral and top boundaries use sponge layers. The sponged zone is 10 km deep from the top and 50 km wide from the lateral boundaries. Over the sponge layer zone, the prognostic variables are relaxed to the basic initial hydrostatic state. The model is integrated for a nondimensional time of  $\frac{\bar{u}t}{a} = 60$  which corresponds to 8.33 hours without diffusion or viscosity.

Fig. 2 shows the numerical and analytic solutions at steady state for the horizontal and vertical velocities, which agree reasonably well. The vertical velocity fields match very closely, although the extrema in the horizontal velocity field are underestimated by the numerical model. The underestimated extrema in the horizontal velocity is also shown in both models of DK83 and Giraldo and Restelli (2008) (hereafter, GR08). And our result in the

horizontal velocity is in good agreement with DK83 and GR08.

Fig. 3 shows the normalized momentum flux values at various times to check vertical transport of horizontal momentum. It is observed that the flux is developing well and the simulations have reached steady-state after  $\frac{\bar{u}t}{a} = 60$ . It is noted that the mean momentum flux at that time is 97% of its analytic value. It agrees well with DK83 as well as GR08; it is important to point out that the Durran-Klemp model is based on the FD method in both directions while the Giraldo-Restelli model is based on SEM in both directions. The mountain test shows the terrain-following vertical coordinate is well suited for the combination of the horizontal SEM and vertical FDM for spatial discretization even though we consider a small mountain.

#### b. 2D density current test

In order to verify the 2DNH's feasibility to control oscillations with numerical viscosity and evaluate numerical schemes in the 2DNH, we conduct the density current test suggested by Straka et al. (1993). The density current test is initialized using a cold bubble in a neutrally stratified atmosphere. When the bubble touches the ground, the density current wave starts to spread symmetrically in the horizontal direction forming Kelvin-Helmholtz rotors. Following Straka et al. (1993) we employ a dynamic viscosity of  $\nu = 75 \text{ m}^2\text{s}^{-1}$  to obtain converged numerical solutions.

For an initial cold bubble, the potential temperature perturbation is given as

$$\theta' = \frac{\theta_c}{2} [1 + \cos(\pi r)], \quad (24)$$

where  $\theta_c = -15 \text{ K}$  and  $r = \sqrt{\left(\frac{x - x_c}{x_r}\right)^2 + \left(\frac{z - z_c}{z_r}\right)^2}$  with the center of the bubble at

$(x_c, z_c) = (0, 3000)$  m. No-flux boundary conditions are used for all boundaries. The model is integrated for 900 s on a domain  $[-25600, 25600] \times [0, 6400]$  m<sup>2</sup>.

Fig. 4 shows the potential temperature perturbation after 900s for 400, 200, 100, and 50m grid spacing ( $\Delta\bar{x}$ ) using 5th order basis polynomials per element. All simulations use  $\Delta\bar{z} = 64$  m grid spacing vertically. As expected, the higher resolution experiments produce better solutions than the lower resolution. At the very lowest resolution of 400 m, only two of the three Kelvin-Helmholtz rotors are generated with somewhat coarsened frontal surfaces. In the experiment with 200 m resolution, the three rotors appear but the numerical solution still suffers from coarsening frontal surfaces. The solutions on grids finer than 100 m converge with the three rotor structures adequately simulated. The converged solution is almost identical to other published solutions (e.g. Straka et al. 1993; Skamarock and Klemp 2008; GR08).

In order to show the effect of higher order of the basis polynomials, we show the potential temperature perturbations using 8th order basis polynomials per element with the same number of degrees of freedom (DOF) of the simulations using 5th order basis polynomials in Fig. 5. The simulation with 8th order basis polynomials on the very lowest resolution of 400 m reproduced the converged solution more closely than with 5th order basis polynomials. Even in the experiment with 200 m resolution, the coarsening frontal surfaces are mitigated and the solution is similar with the converged solution with three rotors.

Fig. 6 shows the profiles of the potential temperature perturbation at the height of 1200 m. The results from the highest grid resolution of the simulations using 5th and 8th order basis polynomials are indistinguishable and well converged (Fig. 6a). Three minima corresponding to the three rotors agree well with other published solutions. In addition to the profiles, the front location (-1K of potential temperature perturbation at the surface), and the



extrema of the pressure perturbation and potential temperature perturbation agree well with each other (Table 1), of which the numbers are comparable to those of GR08. In the numerical results from the different grid resolutions simulated by using 5th order basis polynomials, the potential temperature profile at the coarsest resolution of 400 m grid shows significant fluctuations (Fig. 6b). That of 8th order polynomials, however, tends to be relieved from the deviation from the converged solution (Fig. 6c). The above results suggest that the numerical solution can be converged more rapidly by using higher order of basis polynomial. Furthermore, the results in this paper show that an adequate convergence can be reached at grid resolutions finer than 200 m.

### c. Inertia-gravity wave test

This test examines the evolution of a potential temperature perturbation  $\theta'$  in a constant mean flow with a stratified atmosphere. This initial perturbation diverges to the left and right symmetrically in a channel with periodic lateral boundary conditions. The inertia-gravity wave test introduced by Skamarock and Klemp (1994) (hereafter, SK94) serves as a tool to investigate the accuracy for NH dynamics. Also we use this experiment to check the consistency of the results with various resolutions. The parameters for the test are the same as those of SK94. The initial state is a constant Brunt-Väisälä frequency of  $N = 0.01/\text{s}$  with surface potential temperature of  $\theta_0 = 300 \text{ K}$  and a uniform zonal wind  $\bar{u} = 20 \text{ m/s}$ . In order to trigger the wave, the initial potential temperature perturbation  $\theta'$  is overlaid to the above initial state and is given as

$$\theta'(x, z) = \theta_c \frac{\sin\left(\frac{\pi z}{z_c}\right)}{1 + \left(\frac{x - x_c}{a_c}\right)} \quad (25)$$

where  $\theta_c = 0.01$  K,  $z_c = 10$  km,  $x_c = 100$  km. The domain is defined as  $(x, z) \in [0, 300] \times [0, 10]$  km<sup>2</sup>. We use periodic lateral boundary conditions and a no-flux boundary conditions for both the bottom and top boundaries. The simulation is performed for 3000s with no viscosity.

Fig. 7 shows the solution  $\theta'$  at the initial time and time 3000 s with a horizontal resolution  $\Delta\bar{x} = 250$  m and a vertical resolution  $\Delta\bar{z} = 250$  m. The figure uses the same contouring interval as in SK94 and Giraldo and Restelli (2008) for comparison. The results are produced with 8th order polynomials per element. We have conducted the 2DNH model with various basis polynomial orders at the same resolution, where the simulated results are found to be very comparable. SK94 give an analytic solution for the case of the Boussinesq equations, but it is only valid for the Boussinesq equations while we use the fully compressible equations in our model. Using the analytic solution only for qualitative comparisons, we find that the extrema of our results are comparable to the analytic values. In comparison with the results of Giraldo and Restelli (2008) in which the fully compressible equations are also used, our results look very similar. Fig. 8 shows the profiles along 5000 m for various horizontal resolutions. All models show consistently identical solutions with the symmetric distribution about the midpoint ( $x = 160$  km) which is the location to which the initial perturbation moved by the horizontal flow of 20 m/s after 3000 s. Even at coarser resolution experiments, it does not exhibit phase errors although the maxima and minima near the midpoint ( $x = 160$  km) are slightly damped. Table 2 shows the extrema of vertical velocities and potential temperature perturbations for the results of various horizontal resolutions after 3000 s. It is noted that all experiments give almost the same values for potential temperature perturbation where these values in the range  $\theta' \in [-1.52 \times 10^{-3}, 2.83 \times 10^{-3}]$  are comparable to other studies (e.g., GR08 and Li et al.

2013). GR08 give the ranges of  $\theta' \in [-1.51 \times 10^{-3}, 2.78 \times 10^{-3}]$  from the model based on the spectral element and discontinuous Galerkin method. Also Li et al. (2013) show  $\theta' \in [-1.53 \times 10^{-3}, 2.80 \times 10^{-3}]$  using the high-order conservative finite volume model which are similar to our results.

#### d. Rising thermal bubble test

We also conduct the rising thermal bubble test to verify the consistency of the scheme in the model to simulate thermodynamic motion (Wicker and Skamarock 1998). This test considers the time evolution of warm air in a constant potential temperature environment for an atmosphere at rest atmosphere. The air that is warmer than the ambient air rises due to buoyant forcing which then deforms due to the shearing motion caused by gradients of the velocity field and eventually shapes the thermal bubble into a mushroom cloud. Because the test case has no analytic solution, the simulation results are evaluated qualitatively.

The initial conditions we use follow those of GR08 in which the domain for the case is defined as  $(x, z) \in [0, 1]^2$  km<sup>2</sup>. We consider no-flux boundary conditions for all four boundaries. The domain is initialized for a neutral atmosphere at rest with  $\theta_0 = 300$  K in hydrostatic balance. A potential temperature perturbation to drive the motion is given as

$$\theta' = \begin{cases} 0 & \text{for } r > r_c \\ \frac{\theta_c}{2} \left[ 1 + \cos\left(\frac{\pi r}{r_c}\right) \right] & \text{for } r \leq r_c \end{cases}, \quad (26)$$

where  $\theta_c = 0.5$  K,  $r = \sqrt{(x - x_c)^2 + (z - z_c)^2}$  with  $(x_c, z_c) = (500, 350)$  m. The model was run for a time of 700 seconds. It should be noted that an explicit second-order diffusion on coordinate surfaces is used with a viscosity coefficient of  $\nu = 1 \text{ m}^2 \text{ s}^{-1}$  for all simulations

of this test. The numerical diffusion is applied for momentum and potential temperature along the horizontal and vertical directions so that it eliminates the erroneous oscillations at the small scale – while this amount of diffusion might seem excessive, it has been chosen because it allows the model to remain stable even after the bubble hits the top boundary.

Fig. 9 shows the potential temperature perturbation, horizontal wind, and vertical wind fields for the simulations of two resolutions of 20 m and 5 m horizontal and vertical grid spacings ( $\Delta x^-$  and  $\Delta z^-$ ), respectively, employing 5th order basis polynomials. In both simulations, the fine structures in the numerical solutions are well depicted with a perfectly symmetric distribution at the midpoint and sharp discontinuities of the fields along boundary lines of the bubble. At lower resolution, however, degradations in the solution are visible in the potential temperature perturbation and vertical wind which are illustrated by fluctuations in the values as well as the concaving contours at the top of the bubble. It is noted that while the numerical solution of the model using the spatially centered FDM of Wicker and Skamarock (1998) shows spurious oscillations in the potential temperature field, the simulations here of 2DNH using the horizontally SEM and vertically FDM is devoid of these oscillations.

We also show the vertical profiles of potential perturbation at  $x = 500$  m after 700 s for various resolutions in Fig. 10. Simulations were run with various resolutions of 5, 10, and 20 m, where the resolutions given are defined for both the horizontal and vertical directions. The results of 10 m and 5 m resolutions are almost identical to each other. The result of the lowest resolution of 20 m, however, shows a somewhat unresolved solution, in which the maximum value is underestimated and the phase shift is depicted. The time series for maximum potential temperature perturbation and maximum vertical velocity are shown in Fig. 11. In all simulations, the maximum vertical velocity increases as the maximum theta perturbation decreases. This shows that the thermal energy of the theta perturbation leads to the

acceleration of the vertical velocity. This result agrees well with the study of Ahmad and Lindeman (2007).

## 6. Summary and Conclusions

The non-hydrostatic compressible Euler equations for a dry atmosphere are solved in a simplified 2D slice (X-Z) framework by using the spectral element discretization (SEM) in the horizontal and the third-order finite difference scheme for the vertical discretization. The form of the Euler equations used here are the same as those used in the Weather Research and Forecasting (WRF) model. We employ a hybrid sigma-pressure vertical coordinate which can be modified exactly to the sigma-pressure coordinate at the level of the actual coding implementation.

For the spatial discretization, the spatial operators are separated into their horizontal and vertical components. In the horizontal components, the operators are discretized using the SEM in which high-order representations are constructed through the GLL grid points by Lagrange interpolations in the elements. Using GLL points for both interpolation and integration results in a diagonal mass matrix, which means that the inversion of the mass matrix is trivial. In the vertical components, the operators are discretized using the third-order upwind biased finite difference scheme for the vertical fluxes and centered differences for the vertical derivatives. The time discretization relies on the time-split third-order Runge-Kutta technique.

We have presented idealized standard benchmark tests for large-scale flows (e.g., linear hydrostatic mountain wave) and for nonhydrostatic-scale flows (e.g., inertia-gravity wave, rising thermal bubble, and density currents). The numerical results show that the present dynamical core is able to produce solutions of good quality comparable to other published

solutions. These tests effectively reveal that the combined spatial discretization method of the spectral element and finite difference method in the horizontal and vertical directions, respectively, offers a viable method for the development of a NH dynamical core. Further research will be continued to couple the present core with the existing physics packages together and extend the 2D slice framework to develop a 3D dynamical core for the global atmosphere where the cubed-sphere grid will be used for the spherical geometry.

*Acknowledgements*

This work was funded by Korea's Numerical Weather Prediction Model Development Project approved by Ministry of Science, ICT and Future Planning (MSIP). The first author thanks Dr. Joseph B. Klemp for sharing his idea for the hybrid sigma-pressure coordinate, and would also like to thank Frank Giraldo for his assistance and his MA4245 course at Naval Postgraduate School which introduced us to the spectral element method. The second author gratefully acknowledges the support of KIAPS, the Office of Naval Research through program element PE-0602435N and the National Science Foundation (Division of Mathematical Sciences) through program element 121670.

## References

- Ahmad, N. and J. Lindeman, 2007: Euler solutions using flux-based wave decomposition. *Int. J. Numer. Meth. Fluids*, 54, 47-72.
- Durran, D. R. and J. B. Klemp, 1983: A compressible model for the simulation of moist mountain waves. *Mon. Wea. Rev.*, 111, 2341-2360.
- Giraldo, F. X., 2001: A spectral element shallow water model on spherical geodesic grids. *Int. J. Numer. Meth. Fluids*, 35, 869–901.
- Giraldo, F. X., and T. E. Rosmond, 2004: A Scalable Spectral Element Eulerian Atmospheric Model (SEE-AM) for NWP: Dynamical Core Tests. *Mon. Wea. Rev.*, 132, 133-153.
- Giraldo, F. X., 2005: Semi-implicit time-integrators for a scalable spectral element atmospheric model. *Quart. J. Roy. Meteor. Soc.*, 131, 2431–2454.
- Giraldo, F. X. and M. Restelli, 2008: A study of spectral element and discontinuous Galerkin methods for the Navier-Stokes equations in nonhydrostatic mesoscale atmospheric modeling: equation sets and test cases. *Journal of computational physics* 227, 3849-3877.
- Giraldo, F. X., J. F. Kelly, and E. M. Constantinescu, 2013: Implicit-Explicit Formulations for a 3D Nonhydrostatic Unified Model of the Atmosphere (NUMA). *SIAM J.*



Sci. Comp. 35 (5), B1162-B1194.

Hundsdoerfer, W., B. Koren, M. van Loon, and K. G. Verwer, 1995: A positive finite-difference advection scheme. *Journal of Computational Physics*, 117, 35-46.

Kelly, J. F. and F. X. Giraldo, 2012: Continuous and discontinuous Galerkin methods for a scalable three-dimensional nonhydrostatic atmospheric model: Limited-area mode. *Journal of Computational Physics*, 231, 7988–8008.

Klemp, J. B., W. C. Skamarock, and J. Dudhia, 2007: Conservative split-explicit time integration methods for the compressible nonhydrostatic equations. *Mon. Wea. Rev.*, 135, 2897-2913.

Lauritzen, P., C. Jablonowski, M. Taylor, and R. Nair, 2010: Rotated versions of the Jablonowski steady-state and baroclinic wave test cases: A dynamical core intercomparison. *J. Adv. Model. Earth Syst.*, 2, Art.#15.

Li, X., C. Chen, X. Shen, and F. Xiao, 2013: A multimoment constrained finite-volume model for nonhydrostatic atmospheric dynamics. *Mon. Wea. Rev.*, 141, 1216-1240.

Park, S. -H., W. C. Skamarock, J. B. Klemp, L. D. Fowler, and M. G. Duda, 2013: Evaluation of global atmospheric solvers using extensions of the Jablonowski and Williamson baroclinic wave test case. *Mon. Wea. Rev.*, 141, 3116-3129.

Satho, M., T. Matsuno, H. Tomita, H. Miura, T. Nasuno, and S. Iga, 2008: Nonhydrostatic icosahedral atmospheric model (NICAM) for global cloud resolving simulations. *Journal of Computational Physics*, 227, 3486-3514.

Skamarock, W. C. and J. B. Klemp, 1994: Efficiency and accuracy of the Klemp-Wilhelmson time-splitting technique. *Mon. Wea. Rev.*, 122, 2623-2630.

Skamarock, W. C., J. B. Klemp, J. Dudhia, D. O. Gill, D. M. Barker, M. G. Duda, X. Y. Huang, W. Wang, and J. G. Powers, 2008: A description of the advanced research WRF version 3. NCAR Tech. Note TN-475+STR.

Skamarock, W. C. and J. B. Klemp, 2008: A time-split nonhydrostatic atmospheric model for weather research and forecasting applications. *Journal of Computational Physics*, 227, 3465-3485.

Skamarock, W. C. J. B. Klemp, M. G. Duda, L. D. Fowler, and S. -H. Park, 2012: A multiscale nonhydrostatic atmospheric model using centroidal Voronoi tessellations and C-grid staggering. *Mon. Wea. Rev.*, 140, 3090-3105.

Straka, J. M., R. B. Wilhelmson, L. J. Wicker, J. R. Anderson, and K. K. Droegemeier, 1993: Numerical solutions of a non-linear density current: A benchmark solution and comparisons. *Int. J. Numer. Methods Fluids*, 17, 1-22.

Taylor, M., J. Tribbia, and M. Iskandarani, 1997: The spectral element method for the shallow water equations on the sphere. *Journal of computational physics* 130, 92-108.

Taylor, M., J. Edwards, S. Thomas, and R. Nair, 2007: A mass and energy conserving spectral element atmospheric dynamical core on the cubed-sphere grid. *J. Phys. Conf. Ser.*, 78(012074)

Thomas, S. J. and R. D. Loft, 2002: Semi-implicit spectral element atmospheric model. *Journal of Scientific Computing*, 17, 339-350.

Thomas, S. J. and R. D. Loft, 2005: The NCAR spectral element climate dynamical core: semi-implicit Eulerian formulation. *Journal of scientific computing*, 25, 307-322.

Wicker, L. J. and W. C. Skamarock, 1998: A time-splitting scheme for the elastic equations incorporating second-order Runge-Kutta time differencing. *Mon. Wea. Rev.*, 126, 1992-1999.

## Table Captions

Table 1. Comparison between the 5th and 8th order polynomials per elements for the density current. The simulations is conducted with  $\Delta\bar{x} = 50$  m and  $\Delta\bar{z} = 50$  m resolution.

Table 2. Comparison of the numerical results for various horizontal resolutions. All simulations use the 8th order polynomials per elements and vertical resolution of  $\Delta\bar{z} = 250$  m.

Table 1. Comparison between the 5th and 8th order polynomials per elements for the density current. The simulations is conducted with  $\Delta\bar{x} = 50$  m and  $\Delta\bar{z} = 50$  m resolution.

Order of polynomials	Front location(km)	$p'_{\max}$ (Pa)	$p'_{\min}$ (Pa)	$\theta'_{\max}$ (K)	$\theta'_{\min}$ (K)
5th	14.77	630.62	-452.79	0.08	-8.87
8th	14.74	626.91	-456.84	0.08	-8.94

Table 2. Comparison of the numerical results for various horizontal resolutions for inertia-gravity wave. All simulations use the 8th order polynomials per elements and vertical resolution of  $\Delta\bar{z} = 250$  m.

Resolution(m)	$w_{\max}$ (m/s)	$w_{\min}$ (m/s)	$\theta'_{\max}$ (K)	$\theta'_{\min}$ (K)
$\Delta\bar{x} = 125$	$2.85 \times 10^{-3}$	$-2.89 \times 10^{-3}$	$2.83 \times 10^{-3}$	$-1.52 \times 10^{-3}$
$\Delta\bar{x} = 250$	$2.80 \times 10^{-3}$	$-2.82 \times 10^{-3}$	$2.83 \times 10^{-3}$	$-1.52 \times 10^{-3}$
$\Delta\bar{x} = 500$	$2.73 \times 10^{-3}$	$-2.73 \times 10^{-3}$	$2.83 \times 10^{-3}$	$-1.52 \times 10^{-3}$
$\Delta\bar{x} = 750$	$2.72 \times 10^{-3}$	$-2.70 \times 10^{-3}$	$2.83 \times 10^{-3}$	$-1.52 \times 10^{-3}$
$\Delta\bar{x} = 1250$	$2.68 \times 10^{-3}$	$-2.62 \times 10^{-3}$	$2.82 \times 10^{-3}$	$-1.52 \times 10^{-3}$

## Figure Captions

FIG. 1. The grid points of columns within an element having four GLL points. The hybrid sigma coordinate are illustrated and the close (open) circles on the solid (dashed) line indicate the location of the variables at layer mid-points (interfaces).

FIG. 2. Steady-state flow of (left) horizontal velocity (m/s) and (right) vertical velocity (m/s) over 1 m high mountain at nondimensional time  $\frac{\bar{u}t}{a} = 60$  with a grid resolution of  $\Delta\bar{x} = 2$  km using 5th order basis polynomials per element and  $\Delta\bar{z} = 375$  m. The numerical solution is represented by solid lines and the analytic solution by dashed lines.

FIG. 3. Vertical flux of horizontal momentum, normalized by its analytic value at several non-dimensional times  $\frac{\bar{u}t}{a}$ . Here  $M$  and  $M_H$  are the momentum flux of the numerical and analytic solution.

FIG. 4. Potential temperature perturbation after 900 s using (a)  $\Delta\bar{x} = 400$  m, (b)  $\Delta\bar{x} = 200$  m, (c)  $\Delta\bar{x} = 100$  m, and (d)  $\Delta\bar{x} = 50$  m grid spacing with 5th order basis polynomials per element. All simulations use  $\Delta\bar{z} = 64$  m grid spacing.

FIG. 5. As in Fig. 4, but with 8th order basis polynomials per element.

FIG. 6. Profiles of potential temperature perturbation after 900 s along 1200 m height: (a) high-resolution simulations using 5th (thin solid line) and 8th (thick solid line) order basis function, (b) simulations using 5th order basis polynomials, and (c) simulations using 8th

order basis polynomials per element. Total number of the degrees of freedom is the same in both 5th and 8th order experiments. All simulations use  $\Delta z^- = 64$  m grid spacing.

FIG. 7. Potential temperature perturbation at the initial time (left) and time 3000s (right) for  $\Delta x^- = 250$  m using 8<sup>th</sup> order basis polynomials per element and  $\Delta z^- = 250$  m.

FIG. 8. The profiles of potential temperature perturbation along 5000 m height for  $\Delta x^- = 125$  m (thick solid line),  $\Delta x^- = 500$  m (thin dashed line) and  $\Delta x^- = 1250$  m (thin solid line) using 8th order basis polynomials per element. All models use  $\Delta z^- = 250$  m.

FIG. 9. Plots of (a,b) potential temperature perturbation (K), (c,d) horizontal wind (m/s), and (e,f) vertical wind (m/s) for the rising thermal bubble test after 700s with (left)  $\Delta x^- = 20$  m and (right)  $\Delta x^- = 5$  m resolution. All simulations use 5<sup>th</sup> order basis polynomials per element and  $\Delta z^- = 10$  m grid spacing. All negative values are denoted by dashed lines and positive values by solid lines.

FIG. 10. Vertical profiles of the potential temperature perturbation at  $x = 500$  m after 700 s for various resolutions:  $\Delta x^-, \Delta z^- = 20$  m (thin solid line),  $\Delta x^-, \Delta z^- = 10$  m (thin dashed line), and  $\Delta x^-, \Delta z^- = 5$  m (thick solid line).

FIG. 11. (top) Domain maximum potential temperature perturbation and (bottom) vertical wind for the rising thermal bubble test. All simulations use the 5th order basis polynomials per element, and the vertical resolutions are the same as the horizontal resolutions.

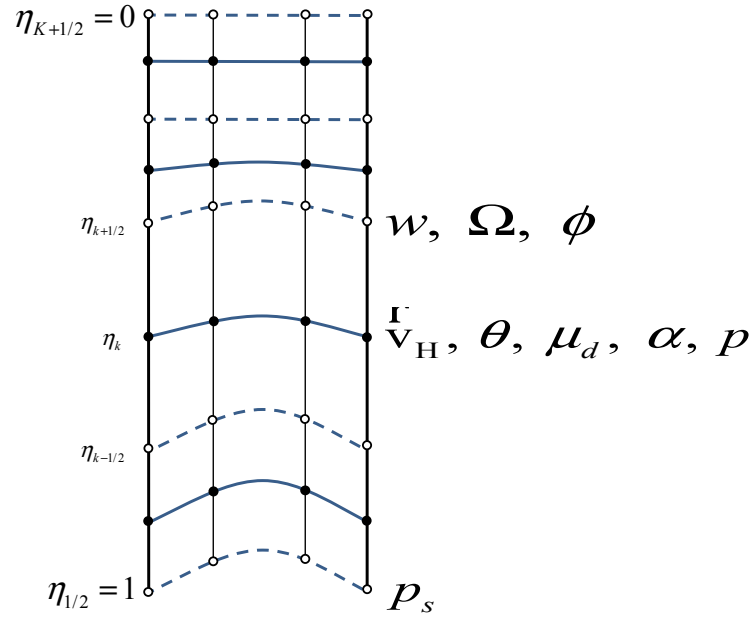


FIG. 1. The grid points of columns within an element having four GLL points. The hybrid sigma coordinate are illustrated and the close (open) circles on the solid (dashed) line indicate the location of the variables at layer mid-points (interfaces).



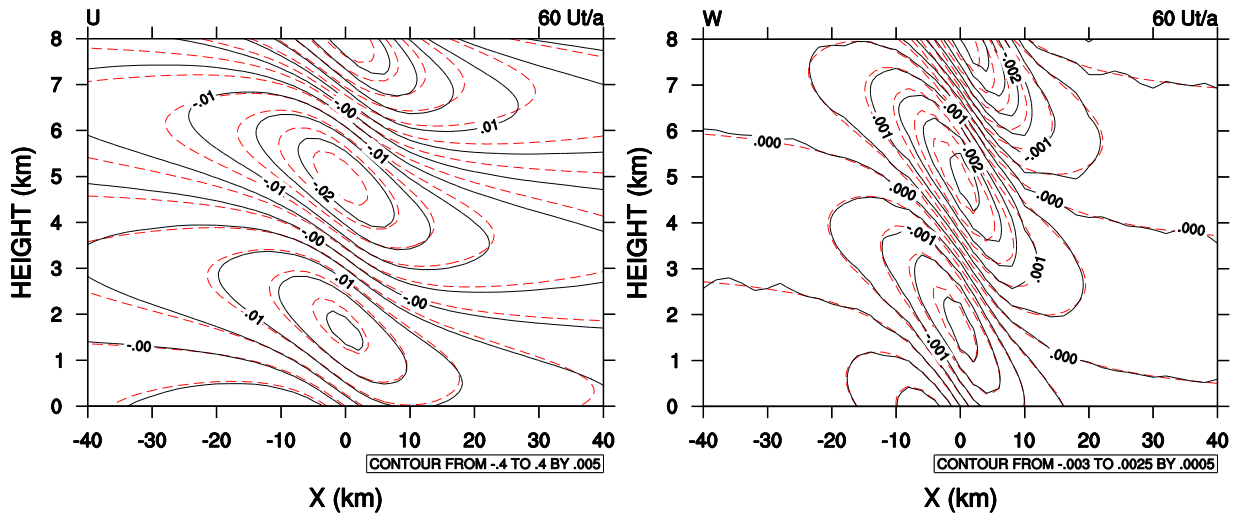


FIG. 2. Steady-state flow of (left) horizontal velocity (m/s) and (right) vertical velocity (m/s) over 1 m high mountain at nondimensional time  $\frac{\bar{u}t}{a} = 60$  with a grid resolution of  $\Delta\bar{x} = 2$  km using 5th order basis polynomials per element and  $\Delta\bar{z} = 375$  m. The numerical solution is represented by solid lines and the analytic solution by dashed lines.

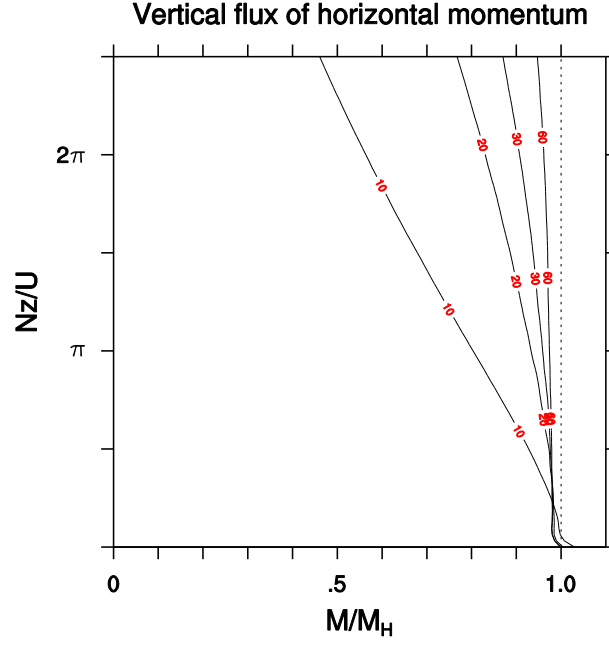


FIG. 3. Vertical flux of horizontal momentum, normalized by its analytic value at several non-dimensional times  $\frac{\bar{u}t}{a}$ . Here  $M$  and  $M_H$  are the momentum flux of the numerical and analytic solutions.

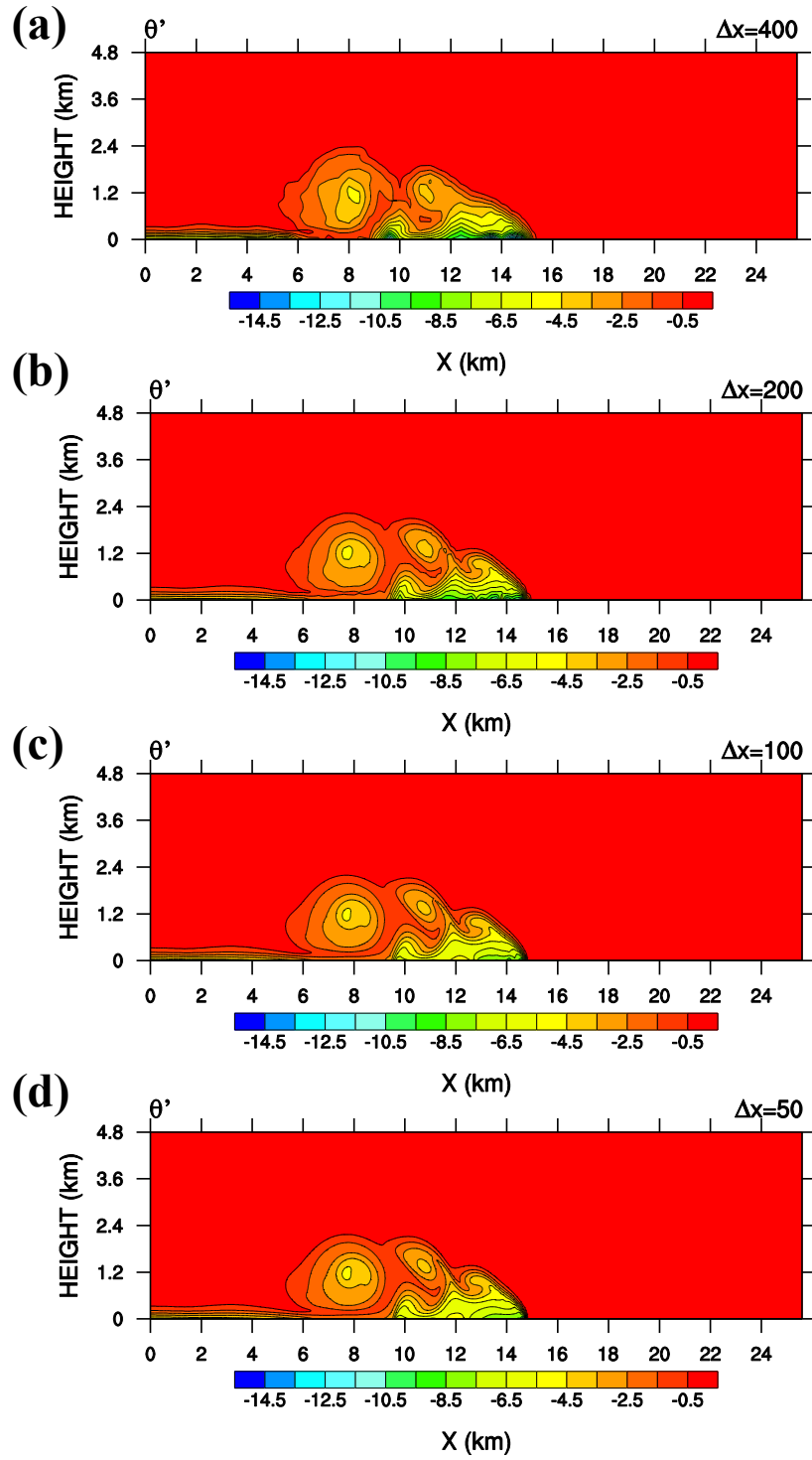


FIG. 4. Potential temperature perturbation after 900 s using (a)  $\Delta \bar{x} = 400$  m, (b)  $\Delta \bar{x} = 200$  m, (c)  $\Delta \bar{x} = 100$  m, and (d)  $\Delta \bar{x} = 50$  m grid spacing with 5th order basis polynomials per element for the density current. All simulations use  $\Delta \bar{z} = 64$  m grid spacing.

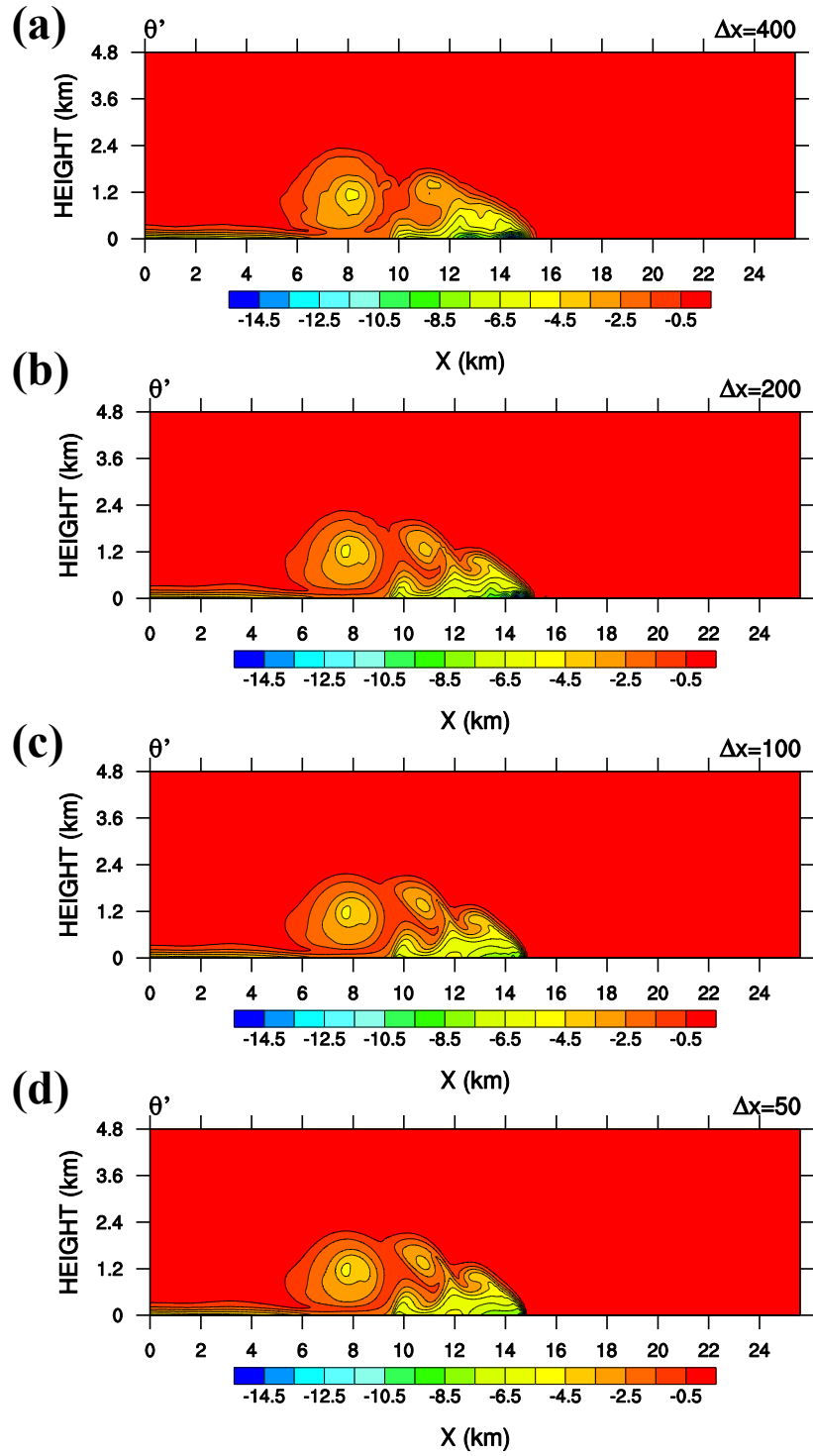


FIG. 5. As in Fig. 4, but with 8th order basis polynomials per element.

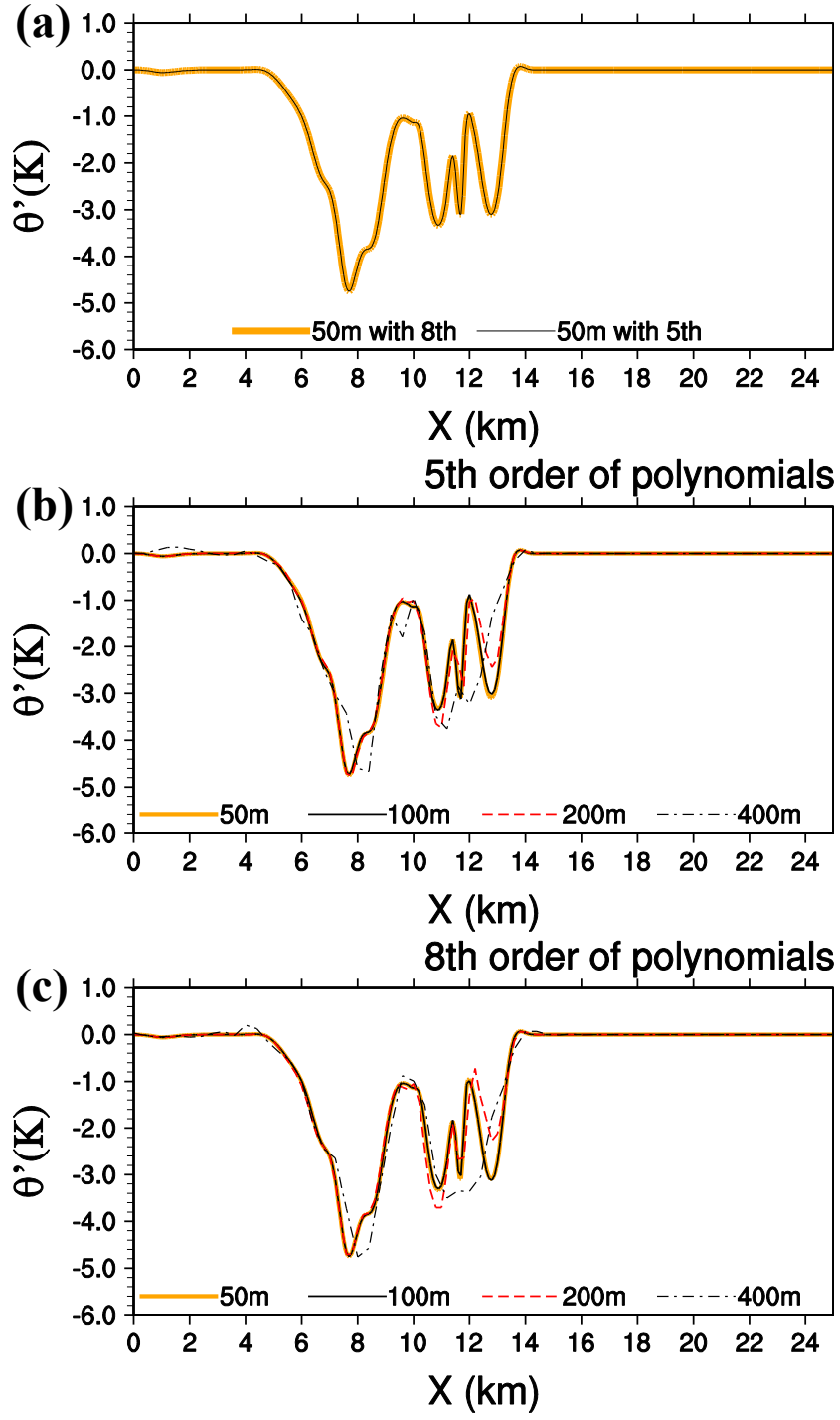


FIG. 6. Profiles of potential temperature perturbation after 900 s along 1200 m height: (a) high-resolution simulations using 5th (thin solid line) and 8th (thick solid line) order basis function, (b) simulations using 5th order basis polynomials, and (c) simulations using 8th order basis polynomials per element. The total number of the degrees of freedom is the same in both 5th and 8th order experiments. All simulations use  $\Delta \bar{z} = 64$  m grid spacing.



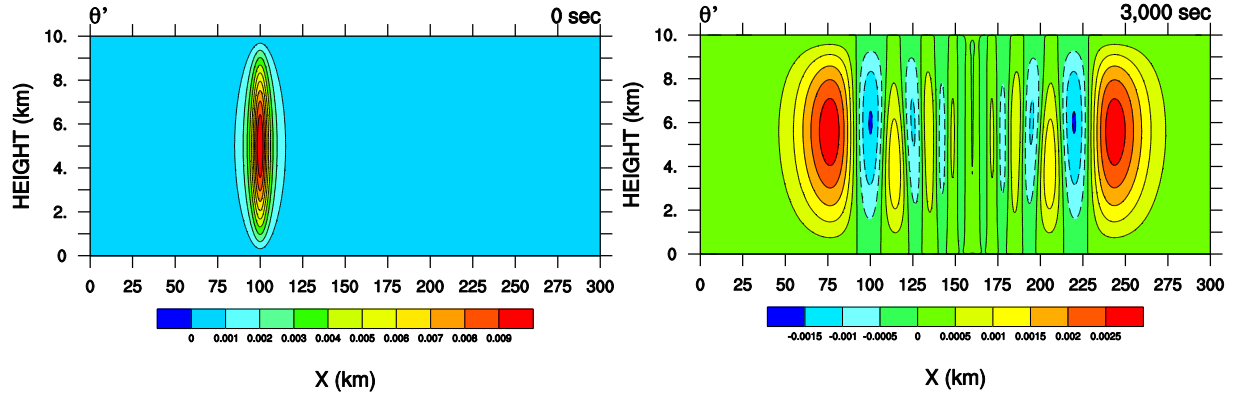


FIG. 7. Potential temperature perturbation at the initial time (left) and time 3000s (right) for  $\Delta\bar{x} = 250$  m using 8<sup>th</sup> order basis polynomials per element and  $\Delta\bar{z} = 250$  m for the inertia-gravity wave.

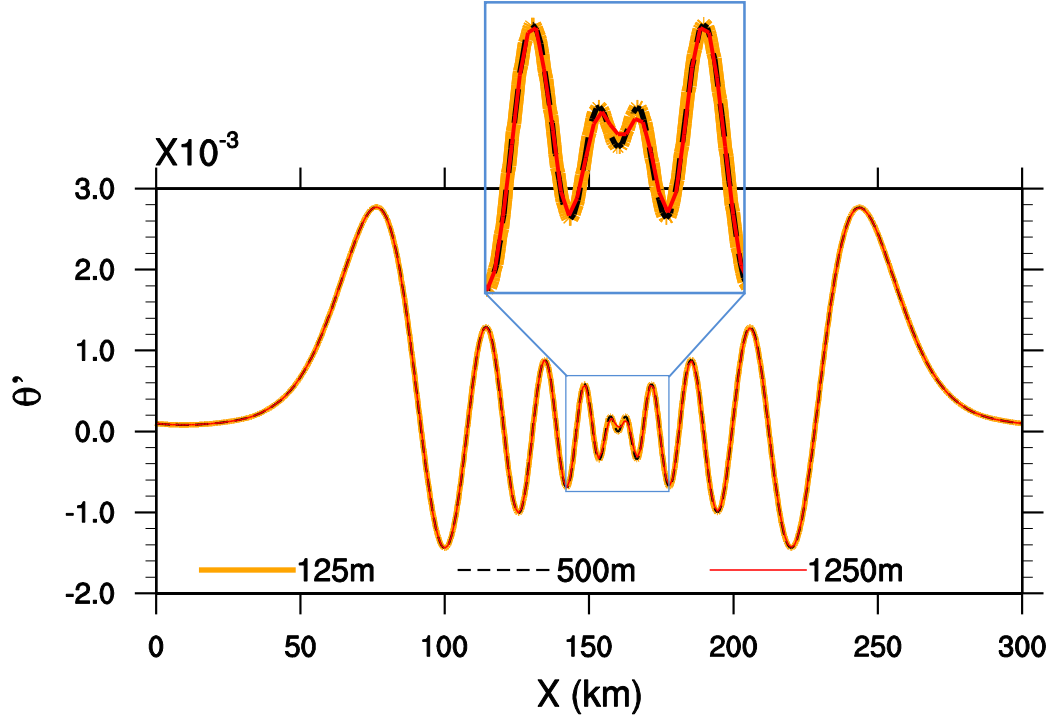


FIG. 8. The profiles of potential temperature perturbation along 5000 m height for  $\Delta\bar{x} = 125$  m (thick solid line),  $\Delta\bar{x} = 500$  m (thin dashed line) and  $\Delta\bar{x} = 1250$  m (thin solid line) using 8th order basis polynomials per element for the inertia-gravity wave. All models use  $\Delta\bar{z} = 250$  m.



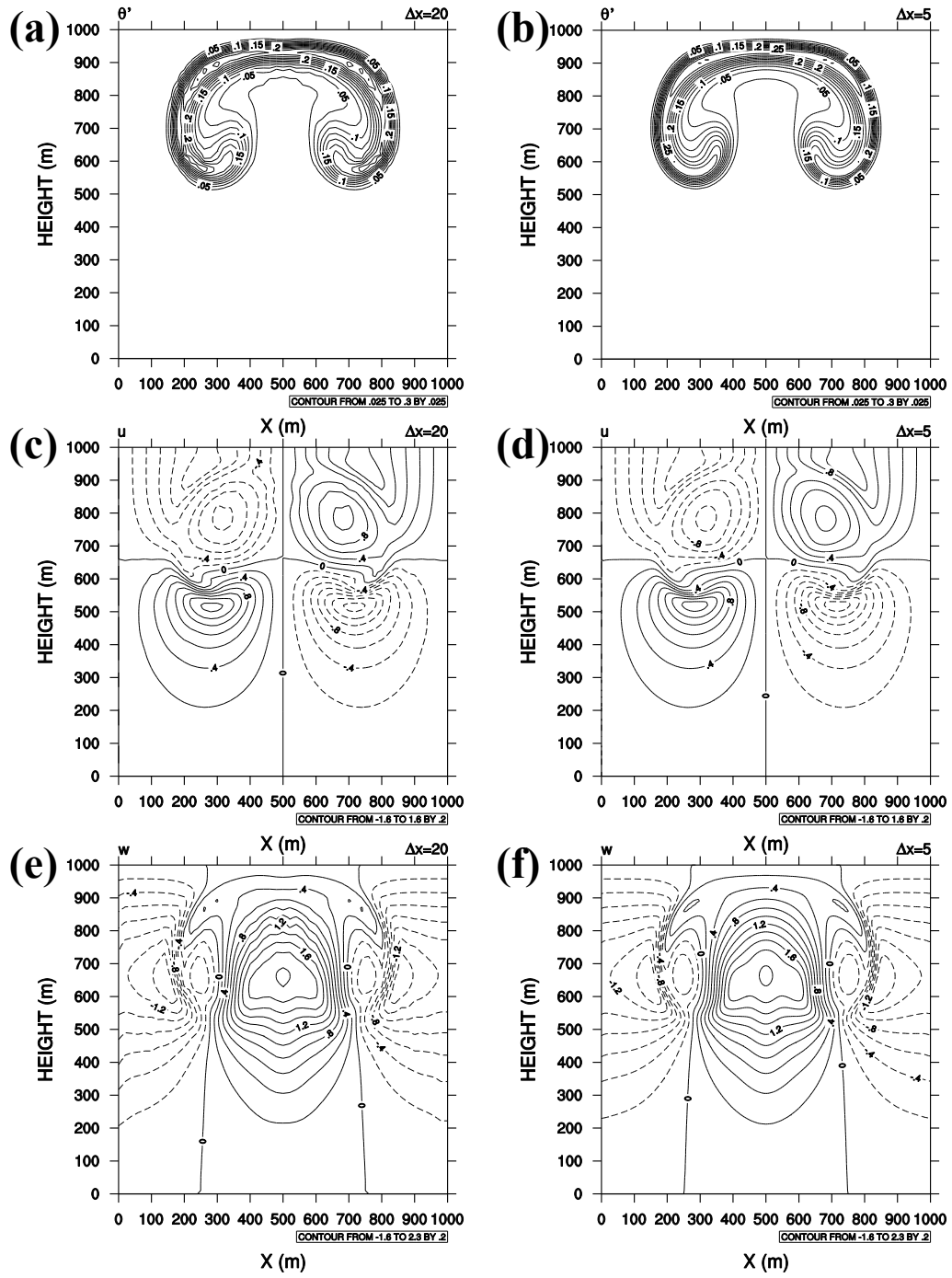


FIG. 9. Plots of (a,b) potential temperature perturbation (K), (c,d) horizontal wind (m/s), and (e,f) vertical wind (m/s) for the rising thermal bubble test after 700s with (left)  $\Delta\bar{x}, \Delta\bar{z} = 20$  m and (right)  $\Delta\bar{x}, \Delta\bar{z} = 5$  m resolution for the rising thermal bubble test. All simulations use 5<sup>th</sup> order basis polynomials per element. All negative values are denoted by dashed lines and positive values by solid lines.

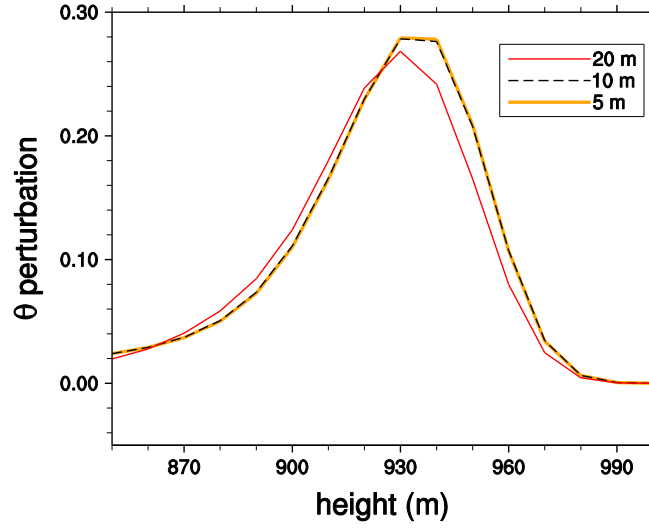
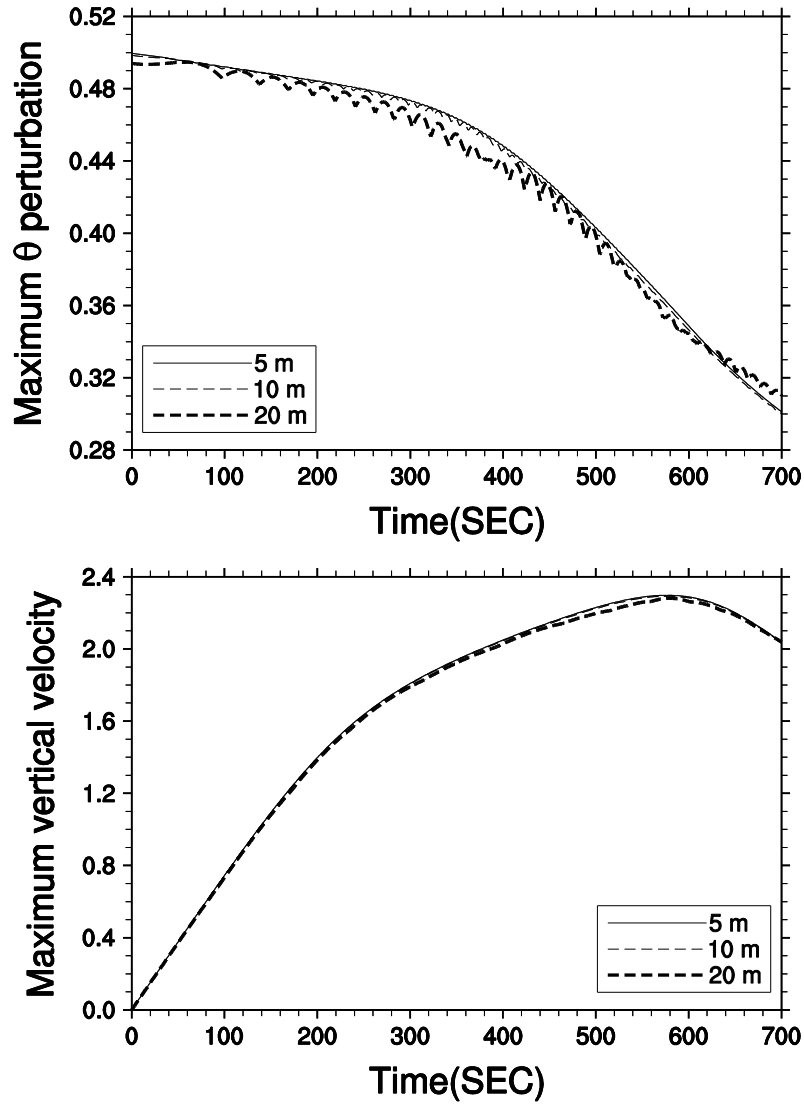


FIG. 10. Vertical profiles of the potential temperature perturbation for the rising thermal bubble test at  $x = 500$  m after 700 s for various resolutions:  $\Delta\bar{x}, \Delta\bar{z} = 20$  m (thin solid line),  $\Delta\bar{x}, \Delta\bar{z} = 10$  m (thin dashed line), and  $\Delta\bar{x}, \Delta\bar{z} = 5$  m (thick solid line).



653

654

655

656

657

FIG. 11. (top) Domain maximum potential temperature perturbation and (bottom) vertical wind for the rising thermal bubble test. All simulations use the 5th order basis polynomials per element, and the vertical resolutions are the same as the horizontal resolutions.